The utilization of ghost reflections retrieved by seismic interferometry for layer-specific characterization of the shallow subsurface

Shirmohammadi, Faezeh; Draganov, Deyan; Ghose, Ranajit

Citation (APA)
Shirmohammadi, F., Draganov, D., & Ghose, R. (2024). The utilization of ghost reflections retrieved by seismic interferometry for layer-specific characterization of the shallow subsurface. *Near Surface Geophysics*, *22*(1), 92-105. https://doi.org/10.1002/nsg.12275

Important note
To cite this publication, please use the final published version (if applicable).
Please check the document version above.

ORIGINAL ARTICLE

Near Surface Geophysics | EAGE EUROPEAN ASSOCIATION OF GEOSCIENTISTS & ENGINEERS

The utilization of ghost reflections retrieved by seismic interferometry for layer-specific characterization of the shallow subsurface

Faezeh Shirmohammadi ⓘ | **Deyan Draganov** | **Ranajit Ghose**

Department of Geoscience and Engineering, Delft University of Technology, Delft, The Netherlands

Correspondence
Faezeh Shirmohammadi, Delft University of Technology, Stevinweg 1, PO Box 5048, 2628 CN Delft, The Netherlands. Email: F.shirmohammadi@tudelft.nl.

Abstract

Seismic interferometry (SI) retrieves the Green function between two receiver locations using their recordings from a boundary of sources. When using sources and receivers only at the surface, the virtual-source gathers retrieved by SI contain pseudo-physical reflections as well as ghost (non-physical) reflections. These ghost reflections are the results of the cross-correlation or auto-correlation (AC) of primary reflections from two different depth levels, and they contain information about the seismic properties of specific layers in the subsurface. We investigated the application of ghost reflections for layer-specific characterization of the shallow subsurface using SI by AC. First, we showed the technique's potential using synthetic data for a subsurface model with a lateral change in velocity, a gradient in depth for velocity, a thickness change and a velocity change of the target layer. Then, we applied the technique to shallow subsurface field data. We also focused on improving the retrieval of ghost reflections by removing the free-surface multiples and muting undesired events in active-source gathers before applying SI. Our results demonstrate that the ghost reflections can be used advantageously to characterize the layer that causes them to appear in the results of SI. Consequently, they can also provide valuable information for imaging and monitoring shallow subsurface structures.

KEYWORDS
seismic, S-wave, reflection, velocity, imaging

INTRODUCTION

Seismic interferometry (SI) is a method for estimating the Green function between different receivers using correlation, convolution or deconvolution of the recordings from surrounding sources by turning the receivers into virtual sources (Snieder et al., 2009; Wapenaar & Fokkema, 2006). In the case of using correlation, the Green function between two receivers is retrieved by cross-correlating recorded responses generated by each source and then summing the correlation results over the surrounding sources. Moreover, Curtis et al.

(2009) showed that it is possible to estimate the Green function between two sources surrounded by a boundary of receivers where one source acts as a virtual receiver.

The theory behind SI assumes certain conditions. Among others, it is assumed that there are no intrinsic losses in the medium, although, in reality, the Earth is strongly attenuating. Additionally, the receivers are presumed to be evenly surrounded by a complete and sufficiently dense boundary of either passive or active sources. In practice, these assumptions are rarely met, particularly when applied to surface exploration data

(i.e. sources and receivers located at or near the surface). As a result, not only the pseudo-physical reflections are retrieved, but also the ghost (non-physical) reflections (Draganov et al., 2010; King et al., 2011; Snieder et al., 2009). The pseudo-physical reflections and lower order multiples are retrieved through the correlation of primary reflections with their surface-related multiples or a multiple with its next-order multiple (Boullenger and Draganov, 2016; Löer et al., 2013). In contrast, ghost reflections are caused by the correlation of primary reflections from two different depth levels (Draganov et al., 2012; King and Curtis, 2012).

The ghost reflections could provide valuable information about the physical rock properties of the subsurface, such as velocity or thickness changes, because they represent reflections from inside specific subsurface layers – as if measured with a virtual ghost source and a virtual ghost receiver positioned directly on top of the specific layers, which means ghost reflections only propagate inside the specific layer (Draganov et al., 2013). Consequently, the ghost reflections can provide information of a specific layer without the effect of changes in overburden and underburden layers. Through realistic numerical modelling using a horizontally layered model, Draganov et al. (2012) showed that ghost reflections are sensitive only to the thickness and velocity of the target layers. Ma et al. (2021, 2022) illustrated the application of ghost reflections in estimating the layer-specific velocity of a fluid–mud layer in a water/fluid–mud system, using ultrasonic experiments. They clearly showed that the retrieved ghost reflections propagate only inside the fluid–mud layer, and the travel paths inside the water layer are eliminated. Moreover, Draganov et al. (2013) applied SI to records from receivers at the Earth's surface from sources in wells. They showed, using a horizontal well, that the identified ghost reflections could be employed to monitor the changes in velocity and quality-factor inside a layer at a depth of 600 m.

In this study, we use numerical modelling and field data to investigate the utilization of ghost reflections retrieved by SI for monitoring and imaging purposes, particularly in shallow subsurface applications. Few studies have investigated the application of ghost arrivals from SI in shallow subsurface studies, especially using field data. Harmankaya et al. (2013) showed the application of ghost arrivals in locating near-surface scatters. To do that, they inverted the travel time of ghost arrivals by solving the inverse problem for several numerically modelled datasets with increasing complexity by including lateral inhomogeneity, and they demonstrated that the location of the scatterer can be estimated with good accuracy from ghost scattered waves. Moreover, Nichols et al. (2010) presented the first application of ghost refractions (the so-called virtual refractions) to field data for near-surface characterization. They determined seismic velocities of unsaturated and saturated

sand layers, and the relative variable depth by combining information from the virtual shot record, the correlation gather and the actual field shot record.

In this paper, we first illustrate the potential of ghost reflections using numerically modelled data for a layered subsurface model in different conditions, including a lateral change in velocity, a gradient change in velocity and a thickness change. We retrieve virtual zero-offset sections using SI by auto-correlation (AC). Studies on retrieving ghost reflections have been mostly restricted to using cross-correlation (CC) in SI. However, the SI by AC can provide extra information on the subsurface in imaging and monitoring, because the result of SI by AC is directly a zero-offset section obtained without any other seismic processing. Additionally, we present the first application of ghost reflections to shallow subsurface field data. The site is located near Rotterdam, the Netherlands. The geology of this site, known from earlier borehole measurements, comprises flat alternating Holocene clay and sand layers (Ghose & Goudswaard, 2004). We retrieve zero-offset sections by turning shots into virtual receivers, and receivers into virtual sources. In both cases, we investigate the trend of ghost reflections for directly imaging and monitoring the target layer.

Ghost reflections usually exhibit similar characteristics to other reflection events, appearing in close proximity to each other with only slight temporal differences. So, one of the most significant challenges in using ghost reflections is their identification. Draganov et al. (2010) showed that ghost reflections could be identified by a change of their polarity after the application of a damping-compensation factor. Curtis and Halliday (2010) showed that ghost arrivals could be identified either through wavefield separation or by reversing the order of the CC in perturbed acoustic media. Draganov et al. (2013) proposed using a vertical-well geometry to identify ghost reflections. Ruigrok et al. (2009) showed that the identification could be achieved by applying both SI by CC with full responses and SI by CC between a full response and only the first arrival at the other receiver.

Here, to address the challenge of identification of the ghost reflections, we eliminate the surface-related multiples in the synthetic dataset, which could be achieved through using an absorbing boundary condition at the surface in the numerical modelling. As a result, the retrieved events include only the ghost reflections. Furthermore, we show how the specific ghost reflections can be retrieved more efficiently by muting undesired reflections in the dataset before applying SI. Using the muted active-source gathers also helps retrieve robust and clear ghost reflections from the field data.

Later, we first present a brief overview of the methodology of retrieving ghost reflections with SI in the METHODS section. Then, in the Numerically modelled data section, we show the results of SI by AC when

applied to data from numerical modelling for several sub-surface models. There we discuss how to retrieve the ghost reflections more efficiently. After that, we illustrate in the Field data section the application of this technique to a field dataset. This is followed by the DISCUSSION and CONCLUSION sections.

METHODS

Through reciprocity theorems of the correlation type, Wapenaar and Fokkemma (2006) showed that the acoustic Green function $\hat{G}(x_B, x_A, \omega)$ between two points at x_A and x_B can be obtained from

$$\hat{G}^*(x_B, x_A, \omega) + \hat{G}(x_B, x_A, \omega) \approx \frac{2}{\rho c} \int_{\partial D} \hat{G}^*(x_A, x, \omega) G(x_B, x, \omega) \, d^2x,$$

(1)

where c and ρ are the constant propagation velocity and mass density, respectively, at and outside of the source-boundary surface ∂D, which effectively encloses x_A and x_B. The asterisk ($*$) denotes complex conjugation in the frequency domain, which corresponds to a time-reversed version of a quantity in the time domain. The right-hand side of relation (1) represents the CC of recordings at points x_A and x_B from active sources at positions x on boundary surface ∂D in the subsurface.

Some assumptions and approximations are made in deriving relation (1): a high-frequency approximation to reduce the integrand to a single CC product; ∂D is a hemisphere with a large radius; the medium at and outside D is homogeneous to remove a term that would otherwise result in the retrieval of a certain type of ghost events (Figure 1a). When the positions x are at the surface, as in a typical active-source exploration survey, the requirement about ∂D to effectively enclose the receivers is not met, leading to ghost reflections being retrieved in the Green function estimates.

Figure 1 shows schematically the retrieval of pseudo-physical and ghost reflections in the virtual-source response for a simple medium. When the sources surround the two receivers, physical reflections (the black arrows in Figure 1a) are retrieved from the correlation of direct arrivals (the dotted blue line in Figure 1a) with their corresponding surface-related multiples (the dotted green line in Figure 1a), where one receiver acts as a virtual source (as indicated by a yellow star in Figure 1a). Here, the free surface acts as a mirror, meaning, through reflection, it turns the half-sphere of sources into a full sphere. As a result, there is a complete surface of sources that surround the receivers, and only physical reflections are retrieved.

The correlation process physically removes the common travel path from the correlated arrivals. The retrieved physical reflection arrivals exhibit kinematics, including the phase, and relative amplitudes coinciding with those of reflections in active-source reflection data.

When the assumptions for obtaining relation (1) are met, also the absolute amplitudes will coincide.

In exploration seismology, where the sources are usually restricted to the surface (such as the red dots in Figure 1b), we can consider that a stationary point on ∂D is equivalent to a stationary point at the surface by using simple geometric arguments (Draganov et al., 2012; Halliday et al., 2007) and applying the stationary-phase method (Snieder et al., 2006). As a result, we can replace the integration over ∂D in relation (1) by a summation over N active sources at the surface (Halliday et al., 2007):

$$\hat{G}^*(x_B, x_A, \omega) + \hat{G}(x_B, x_A, \omega) \propto \sum_{n=1}^{N} \hat{G}^*(x_A, x_n, \omega) \hat{G}(x_B, x_n, \omega).$$

(2)

The right-hand side of this relation is, in the time domain, a CC between two observations at positions x_A and x_B, both originating from active sources located at x_n at the surface (such as the red dots in Figure 1b). The retrieved Green function on the left-hand side of relation (2) comprises pseudo-physical reflections, as well as ghost reflections. These ghost reflections are retrieved in the time domain from the CC of the primary reflections from two different interfaces due to insufficient destructive interferences (Draganov et al., 2012; Ma et al., 2022). Ghost reflections are similarly retrieved from the correlation of internal multiples with primaries or other internal multiples. For example, the result of CC of the primary reflection from the second interface recorded at x_B (the orange arrows in Figure 1b) with the primary reflection from the first interface (the blue arrows in Figure 1b) retrieves a ghost reflection which propagates only inside the second layer (the cyan arrows in Figure 1b). The retrieved ghost reflection can be intuitively interpreted as the wavefield reflected from the second interface as though a ghost virtual source (the red star in Figure 1b) and a ghost virtual receiver (the white triangle in Figure 1b) are positioned at the first interface. We labelled them as a ghost virtual source or a ghost virtual receiver because they cannot be physically placed there. Note that the retrieved pseudo-physical reflection arrivals exhibit kinematics coinciding with those of reflection events in active-source reflection data, but the amplitudes and phases are not directly comparable. So, they are labelled pseudo-physical reflections (Löer et al., 2013; Boullenger & Draganov, 2016).

In relation (2), if we substitute the response x_A instead of x_B on the right-hand side, the retrieved Green function on the left-hand side is the result of AC of the arrivals at receiver x_A, which means x_A acts as a co-located virtual source and receiver:

$$\hat{G}^*(x_A, x_A, \omega) + \hat{G}(x_A, x_A, \omega) \propto \sum_{n=1}^{N} \hat{G}^*(x_A, x_n, \omega) \hat{G}(x_A, x_n, \omega).$$
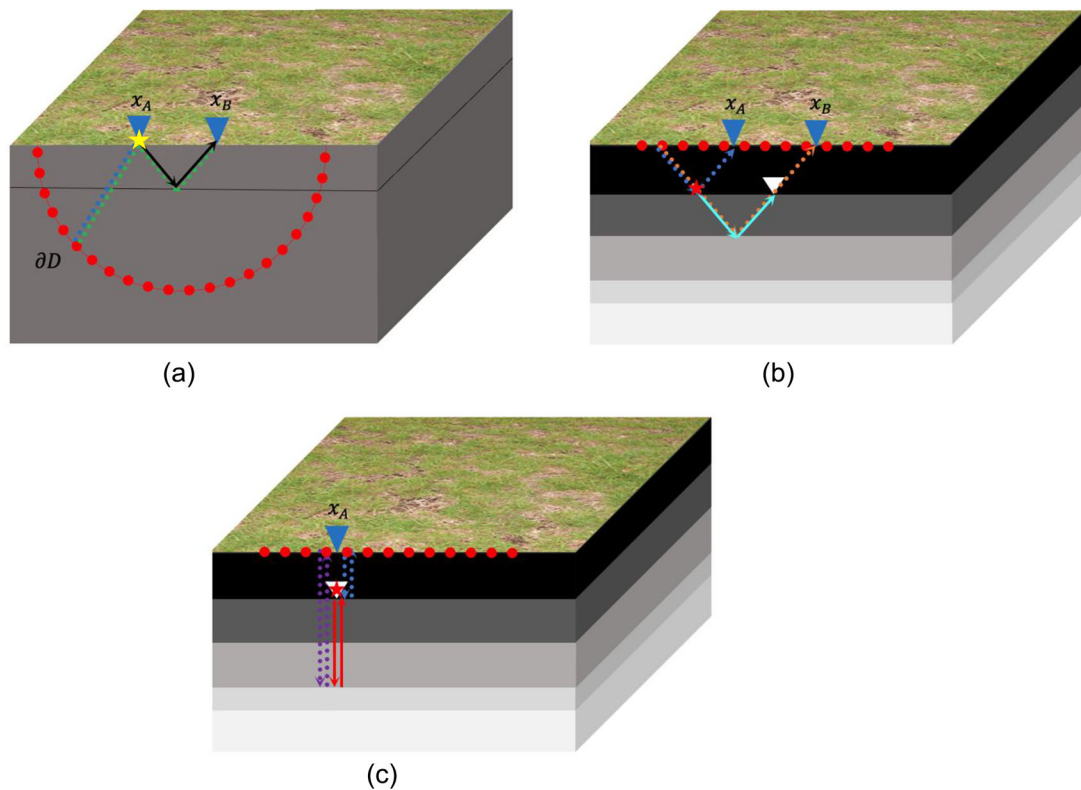
(3)

FIGURE 1 Schematic representation of seismic interferometry (SI). (a) The sources (the red dots) are at the source-boundary surface ∂D, which effectively encloses the receivers at x_A and x_B (blue triangles) due to the Earth's free surface. The retrieved virtual-source response contains physical reflections (the black arrow) from the cross-correlation (CC) of a direct arrival (the blue dotted line) with its surface-related multiple (the green dotted line). The yellow star indicates the virtual source. (b) The sources are on the surface. The retrieved virtual-source response includes pseudo-physical and ghost reflections (e.g. the cyan arrows), in which the ghost reflection is the result of the CC of the primary reflection from the top and the bottom of the second layer (the blue and orange dotted arrows). (c) Same as (b) but for SI by auto-correlation (AC). The retrieved virtual-source response includes pseudo-physical and ghost reflections (e.g. the red arrows), in which the ghost reflection is the result of the cross-correlation (CC) of the primary reflections from the bottom of the first and the bottom of the third layer (the blue and purple dotted arrows). The red star indicates the ghost virtual source, and the white triangle indicates the ghost virtual receiver.

Similar to CC, besides the pseudo-physical reflections, ghost reflections are also retrieved. The retrieved ghost reflection propagates inside a specific layer which represents a reflection for a ghost virtual source to a receiver co-located exactly at the top of that specific layer. Besides the specific ghost reflection which propagates inside one layer, it is possible to retrieve ghost reflections from inside multiple layers, for example the ghost reflection from inside the second and the third layers in Figure 1c (the red arrows). This retrieved ghost reflection is the result of the correlation of the primary reflections from the bottom of the first layer (the blue arrows in Figure 1c) and the bottom of the third layer (the purple arrows in Figure 1c), and it propagates vertically as the layers are horizontal.

The retrieved ghost reflection in Figure 1c (the red arrows) represents a zero-offset reflection arrival. If we use multiple surface receivers at the surface as x_A in relation (3) and repeat the AC and summation process, the result is a virtual zero-offset section which provides

an image of specific subsurface structures directly in two-way travel time.

RESULTS

In this section, we first use numerically modelled data to demonstrate how the ghost reflections can be used for monitoring purposes of shallow subsurface structures. We discuss the results of SI by AC for different conditions of the subsurface model. Second, we show the method's applicability to a shallow subsurface field dataset.

Numerically modelled data

We illustrate the potential of SI on data derived from numerical modelling using a shallow subsurface structure from around Rotterdam, the Netherlands (Ghose & Goudswaard, 2004). Figure 2a shows the subsurface
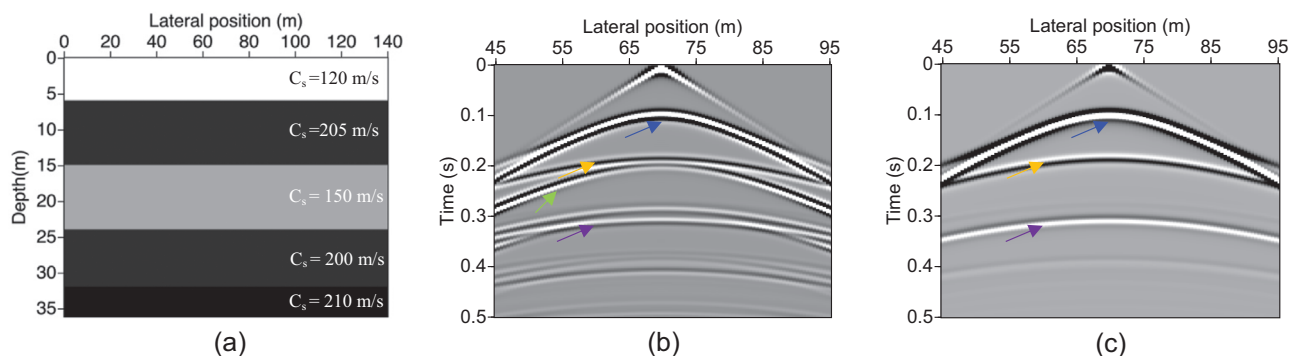
FIGURE 2 (a) Shear-wave velocity (C_S) model for the base survey; (b) directly modelled reflection response for an active source at (70,0) m, (c) the same as (b) but when the model has an absorbing boundary condition at the surface. The colour-coded arrows indicate the events described in Table 1.

TABLE 1 Colour coding of events in the directly modelled reflection response and in the result from seismic interferometry (SI) in Figures 1–4.

Colour codes in Figures 1–4	Explanation
Blue	Primary reflection from the bottom of the first layer
Orange	Primary reflection from the bottom of the second layer
Purple	Primary reflection from the bottom of the third layer
Green	Surface-related multiple from the bottom of the first layer
Yellow	Combination of pseudo-physical reflections and ghost reflections
Cyan	Ghost reflection from inside the second layer
Pink	Ghost reflection from inside the third layer
Red	Ghost reflection from inside the second and third layers

model, which consists of five horizontal layers below a free surface.

The fixed receivers were placed from 45.25 m to 95.25 m, and the sources were placed from 30 m to 110 m at the free surface with spacing between neighbouring points of 0.5 m and 1.0 m, respectively. A Ricker wavelet with a centre frequency of 45 Hz was used as a source signature, and a finite-difference modelling code (Thorbecke & Draganov, 2011) in an acoustic mode generates the seismic reflection dataset. This approach is valid as we imitate a 2D field survey for which the shear (SH)-wave sources and the horizontal-component receivers are oriented in the direction perpendicular to the line. Because of this orientation and assuming no 3D scattering, the horizontally polarized SH waves which we record are completely decoupled from the compressional and vertically polarized SH waves.

Figure 2b shows the modelled common-source gather for a source located at 70 m. Next to the primary reflections, such as the reflections from the bottom of the first (the blue arrows), second (the orange arrows) and third (the purple arrows) layer, also free-surface multiples are present in the shot gather, such as the free-surface multiple of the first layer (the event indicated by the green arrow in Figure 2b). Table 1 lists the colours correspond-

ing to events in the directly modelled reflection response and the result from SI in Figures 1–4.

We applied SI by AC (relation 3) to the simulated reflection dataset, such as the active-source gather in Figure 2b, to investigate the retrieval of the ghost reflections, which means that we correlated each signal with itself. Consequently, the zero-offset sections can be retrieved at each receiver location. The virtual zero-offset sections (Figure 3) perfectly match the geometry of the specific subsurface interfaces. In our numerical modelling, the subsurface model is horizontal. Therefore, we retrieve the horizontal events in the results of SI by AC, and it is easier to separate different reflections and interpret them. To enhance the clarity of the depicted events in the virtual zero-offset sections, we also show the trace of one receiver at 70.25 m in Figure 3.

Figure 3a shows the virtual zero-offset section when full active-source gathers are used in SI by AC. We retrieved several horizontal reflections, including pseudo-physical and ghost reflections such as the events shown by the cyan, orange, blue and purple arrows. But identifying all ghost reflections is challenging when the full recordings are used for SI by AC, because different retrieved arrivals interfere with each other.

One way to make the result from SI by AC clearer for the interpretation of the ghost reflections is to mute
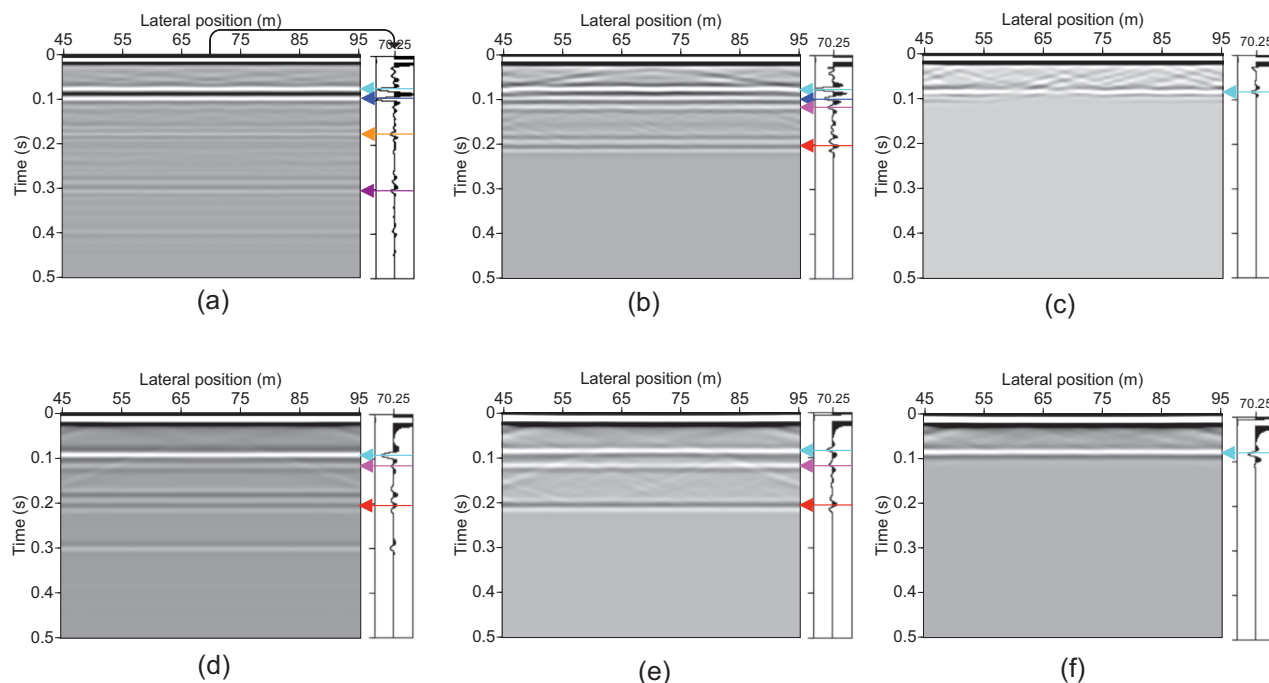
FIGURE 3 Retrieved results of the application of seismic interferometry (SI) by auto-correlation (AC) to **(a)** the full active-source gathers, **(b)** the active-source gathers, which are muted before the reflection from the bottom of the first layer and after the reflection from the bottom of the third layer, **(c)** the active-source gathers which are muted before the reflections from the bottom of the first layer and after reflection from the bottom of the second layer, **(d–f)** same as (a–c) but when the model has an absorbing boundary condition at the surface. The seismic trace next to each image represents the retrieved result for the receiver located at 70.25 m. The colour-coded arrows indicate the events described in Table 1.

the arrivals recorded before and after the reflections that contribute to the retrieval of specific target ghost reflections. Figure 3b shows the virtual zero-offset section when we manually muted all events before the reflection from the bottom of the first layer (the arrival indicated by the blue arrow in Figure 2b) and after the reflection from the bottom of the third layer (the arrival indicated by the purple arrow in Figure 2b). As we can see in Figure 3b, we retrieved better the ghost reflections inside the third layer at approximately 0.12 s (the pink arrow) or the ghost reflection from the combination of the second and third layers with an arrival time at approximately 0.21 s (the red arrow). However, the ghost reflection from inside the second layer is unclear (the cyan arrow in Figure 3b). The two-way travel time of each of these ghost reflections corresponds to a specific layer velocity and thickness. For example, the ghost reflection at 0.21 s traverses the second and the third layers, so its two-way travel time is characterized by the effective velocity of these two layers.

To retrieve the specific ghost reflection that propagates only inside the second layer, we muted the arrivals before the reflection from the bottom of the first layer and after the reflection from the bottom of the second layer in the active-source gathers (the arrivals indicated in Figure 2b by blue and orange arrows, respectively) before applying SI by AC. As shown in Figure 2b, muting

all unwanted events, such as all direct arrivals at far offsets, is difficult. However, this has very little impact on the result of SI as the direct-wave energy is already weak, and we perform stacking over all active-source gathers. By muting, we expected to retrieve the ghost reflection from the correlation of the primary reflections from the top and bottom of the second layer, which propagates only inside the second layer as if measured from a ghost virtual source to ghost virtual receivers – both placed directly at the top of the second layer.

Figure 3c shows the virtual zero-offset sections derived from the application of SI by AC using the thus-mutated active-source gathers. We see a clear event at 0.09 s, which is the ghost reflection from inside the second layer (the cyan arrow). Some artefacts are observed because it is impossible to mute all undesired reflections for some active-source gathers, especially for the far offsets. Moreover, the primary reflections may be contaminated with free-surface multiples.

As mentioned above, it is still challenging to discriminate all ghost reflections from the pseudo-physical reflections in the results of SI. A better way of achieving this discrimination is to remove the free-surface multiples in the active-source gathers. This precludes retrieval of pseudo-physical reflections and leads to retrieval of only ghost reflections. In numerical modelling, removing the free-surface multiples is easily
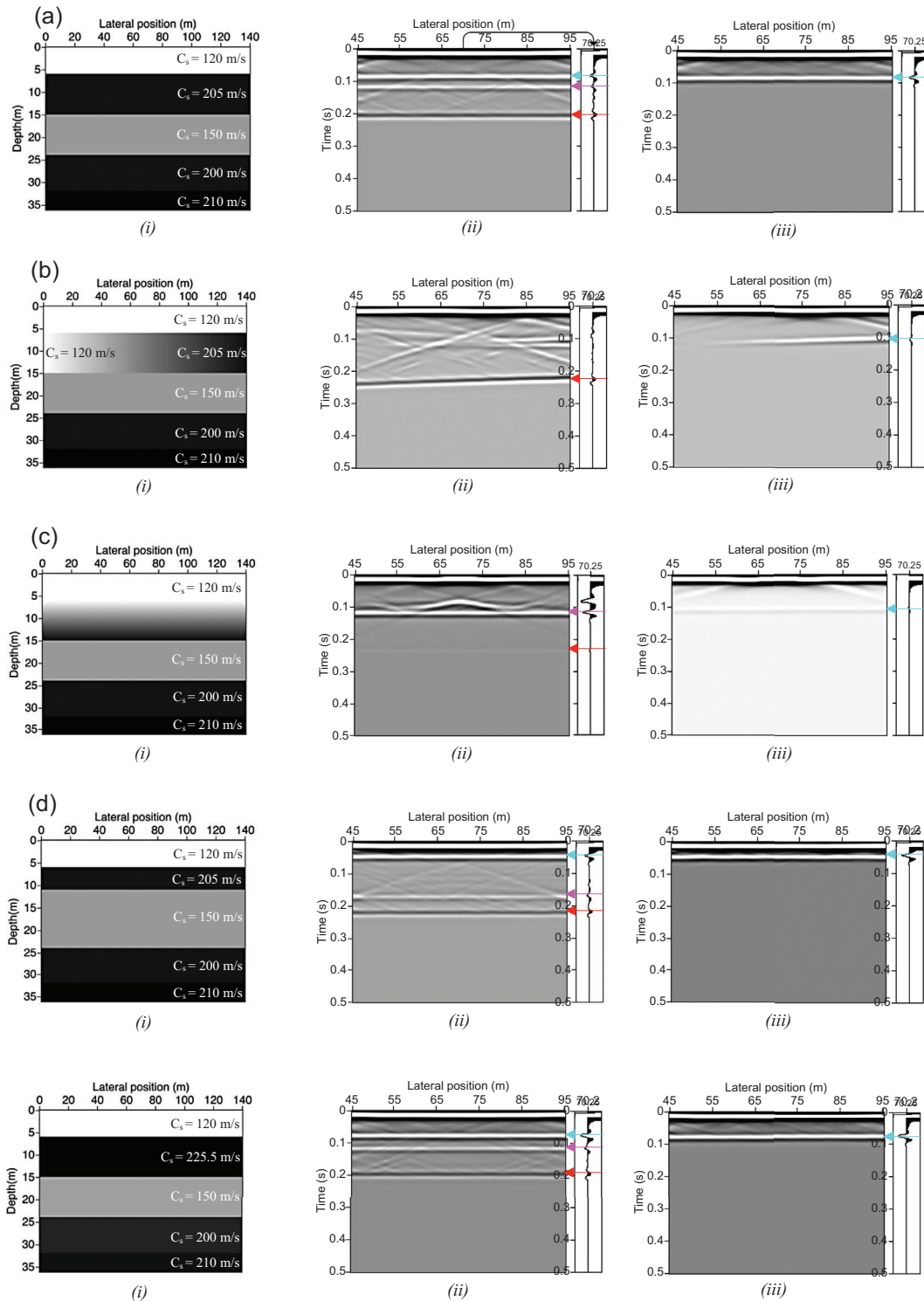
FIGURE 4 (i) Shear-wave velocity (C_S) subsurface models used to test the idea of monitoring in case of (a) a base subsurface model, (b) a lateral change in the velocity of the second layer, (c) a gradient change with depth in the velocity of the second layer, (d) a thickness change in the second layer, (e) a 10% velocity change in the second layer. (ii) Retrieved results of seismic interferometry (SI) by auto-correlation (AC) applied to active-source gathers in which events before the reflections from the bottom of the first layer and after the reflection from the bottom of the third layer are muted for the subsurface models in (i), respectively. (iii) Same as (ii), but SI by AC applied to active-source gathers which were muted before the reflections from the bottom of the first layer and after the reflection from the bottom of the second layer. The seismic trace next to each represents the retrieved result for the receiver located at 70.25 m, and the colour-coded arrows indicate the events described in Table 1.

achieved by defining an absorbing boundary condition at the surface. With this condition, we have only the primaries in the active-source gathers. In field data, it is possible to use surface-related multiples elimination (SRME) (Verschuur, 1991) or estimate the primaries through sparse inversion (van Groenestijn & Verschuur, 2009), which are the two most widely accepted tools for free-surface-multiple elimination.

Figure 2c shows the common-source gather for an active source located at 70 m, when the absorbing boundary condition is used at the surface. The primary reflections from the bottom of all layers are observable (the blue, orange and purple arrows in Figure 2c). By applying SI to such gathers, we retrieve only ghost reflections. Figure 3d shows the zero-offset section retrieved from SI by AC when we define an absorbing boundary condition at the surface. As shown in this figure, we retrieve all ghost reflections from inside all the layers, or the ghost reflections from inside more than one layer. Consequently, it is not easy to separate the specific ghost reflections. Therefore, we used the muted active-source gathers before correlation. Figure 3e shows the result of SI by AC when we used the muted active-source gathers containing only the reflection from the bottom of the first, second and third layers. We retrieved better the ghost reflection inside the second, third and from inside the second and the third layers together (the cyan, the pink and the red arrows, respectively, in Figure 3e) in comparison with Figure 3d. Moreover, by removing the surface-related multiples in the active-source gathers, we retrieved stronger the ghost reflections, compared to those in Figure 3b.

Figure 3f shows the virtual zero-offset section resulting from SI by AC using muted active-source gathers that contain reflections only from the top and bottom of the second layer. The event around 0.09 s is the ghost reflection from inside the second layer. By comparing with Figure 3c, which results from SI by AC using the subsurface model with a free surface at the top, we can see that the retrieved ghost reflection is more robust.

To investigate the application of ghost reflections for monitoring in specific subsurface structures, we looked into retrieving the ghost reflections for different subsurface models shown in Figure 4a–e. Our target layer for monitoring is the second layer. The five models in Figure 4 include a base subsurface model (Figure 4a(i)) lateral change in velocity in the second layer (Figure 4b(i)), a gradual change of velocity with depth in the second layer (Figure 4c(i)), a thickness change of the second layer (Figure 4d(i)) and finally a 10% velocity increase in the second layer (Figure 4e(i)). We applied SI by AC (relation 3) to the modelled active-source reflection responses for these subsurface models. Based on the results of SI by AC using the base survey (Figure 3), we focused on the result of SI by AC for the muted active-source gathers with an absorbing boundary condition at the surface.

Figure 4a–e(ii) shows the result of SI by AC for the base subsurface models and the other subsurface models with an absorbing boundary condition at the surface, when we use active-source gathers muted to contain reflections from the bottom of the first, second and third layers. Figure 4a(ii) shows the result of the model for the base survey. This figure shows that, as shown also earlier, we could retrieve the ghost reflection inside the second layer (the cyan arrow), the ghost reflection inside the third layer (the pink arrow) and also the ghost reflection from the combination of these two layers (the red arrow). Similar to Figure 3, we have included a single trace from the receiver positioned at 70.25 m to provide a more detailed depiction of the indicated events.

Figure 4b(ii) shows the result of SI by AC for the model with a lateral velocity change in the second layer. The ghost reflection of the combination of the second and the third layers is clear at approximately 0.24 s at the horizontal distance of 45 m (the red arrow). It is not possible to distinguish the ghost reflection from inside the second layer and the ghost reflection from inside the third layer clearly. Moreover, for the model with a gradient change of velocity with depth in the second layer, it is difficult to see the ghost reflection inside the second layer. Again, the ghost reflection inside the third layer (the pink arrow in Figure 4c(ii)) and the combination of the second and the third layers (the red arrow in Figure 4c(ii)) are clearer.

Figure 4d(ii) shows the result of SI by AC for a thickness change in the second layer, whereas Figure 4e(ii) shows the result of SI by AC for a 10% velocity change inside the second layer. In both cases, we retrieved the ghost reflection inside the second and the third layers (the cyan and the pink arrows, respectively) and the ghost reflection from inside these two layers (the red arrow in Figure 4d(ii),e(ii)).

By comparing the SI result in Figure 4a–e(ii), it is obvious that the ghost reflection from inside the second and the third layers (the red arrow) can be used for monitoring purposes, because the differences in time and amplitude as a result of respective changes in the subsurface models are clearly recognizable. However, retrieving the ghost reflections from inside the second layer (the cyan arrow in Figure 4a–e(ii)) is more challenging with this type of muting because of the interference with the ghost reflection inside the third layer. Nevertheless, the ghost reflection from inside the second layer is recognizable, as indicated by the cyan arrow, and it reveals changes in comparison with the base model (Figure 4a(ii)) for the case of the thickness change (Figure 4d(ii)) and the velocity change (Figure 4e(ii)).

As all changes occur in the second layer of our subsurface models, we further focus on retrieving the ghost reflection from inside the second layer, resulting from the correlation of the primary reflection from the top and the bottom of the second layer. As explained above, we used muting before the reflection from the top of the

second layer and after the reflection from the bottom of the second layer and then applied SI by AC.

Figure 4a–e(iii) shows the result of SI by AC applied to the muted active-source gathers. We retrieved only the ghost reflection from inside the second layer (the cyan arrow in Figure 4a–e(iii)) – we retrieved a clear and robust arrival at 0.09 s for the base survey (Figure 4a(iii)). For the model with a lateral change, we can see that the retrieved ghost reflection has a weak amplitude at a place where it is expected, that is at shorter lateral distances (Figure 4b(iii)). Figure 4c(iii) shows the ghost reflection from inside the second layer of the model with a gradient change of velocity in depth. The retrieved ghost reflection has a lower amplitude than in Figure 4d(iii). Figure 4e(iii) shows the result of SI by AC in the case of thickness change. We see the ghost reflection from inside the second layer at around 0.05 s, which corresponds with the two-way travel time inside the second layer. In the case of a velocity change of 10% (higher than that in the base-survey model), the ghost reflection from inside the second layer shows a time difference of approximately 0.008 s (Figure 4e(iii)). For a comparison of the retrieved ghost reflection from inside the second layer, we conclude that the use of layer-specific ghost reflection does allow monitoring the change in thickness and/or velocity of or inside the second layer.

Field data

After showing the usefulness of retrieving ghost reflections from SI using the numerically modelled data for the five subsurface models, we next test the technique on field data.

The site where the data were recorded is located in the western part of the Netherlands, near Rotterdam. The total profile length was 190 m with shot and receiver interval of 1.0 and 0.5 m, respectively. The sources and receivers moved along a line following an end-on acquisition geometry, which means that the receivers are positioned on the right-hand side of each shot. As SH-wave source, a high-frequency electrodynamic horizontal vibrator (Brouwer et al., 1997; Ghose, 2012; Ghose et al., 1996) oriented in the direction perpendicular to the line was used. The receivers recorded the horizontal particle velocity also in a direction perpendicular to the line. Therefore, we could directly apply to the recorded data the methodology described in the previous subsection.

The geology of this site, known from earlier borehole measurements, comprises flat alternating layers of Holocene clay and sand (Figure 5a,b). The sand is relatively homogeneous. In the topmost part (Holocene), the appearances of sand layers at around 1–2 m, 4–5 m and 7–12 m depths were marked in several boreholes (Ghose & Goudswaard, 2004).

Figure 5c shows one example of the recorded shot gathers after the application of a pre-processing step, which also included surface-wave suppression via SRME (Verschuur, 1991). Ghose and Goudswaard (2004) illustrated the successful application of SRME on this shallow SH-wave field dataset. Several strong reflection events are visible in the gather corresponding to various sand-clay interfaces. Some examples of raw and pre-processed shot gathers can be found in Figure 5 of Ghose and Goudswaard (2004).

We illustrated in the previous section that, to retrieve better the ghost reflections from inside a specific layer, it is better to use the dataset without surface-related multiples. Therefore, we used the recorded data after the application of the free-surface-related multiple elimination. Moreover, to retrieve a specific ghost reflection, we used tapered muting to extract only the two of the earliest reflections from the active-source gathers (indicated by the transparent blue area in Figure 5c).

We applied SI by AC to all available active-source gathers from these data. We used SI not only to turn sources into virtual receivers (Figure 6a) but also to turn the receivers into virtual sources (Figure 6b). When we turn the sources into virtual receivers, we sum the AC results over the receivers whose spacing is 0.5 m. The so-retrieved zero-offset section is more reliable, because the spacing of the stacked traces is shorter than the dominant wavelength. When we turn the receivers into virtual sources, we sum over the available sources whose spacing is 1.0 m. In this case, the spacing is similar to the dominant wavelength, but there are more traces in the ghost zero-offset section, because there are more receiver points than source points. Comparing the result in Figure 6a to that in Figure 6b, we ascertain the validity of the latter. Thus, for interpretation, we use both results. Note that the retrieval of ghost reflections eliminates any surface statics. Therefore, we have similar ghost reflections in Figure 6a,b, despite the fact that we use common-source and common-receiver gathers, respectively.

The ghost zero-offset sections in Figure 6 exhibit a ghost reflection at approximately 20 ms (as indicated by the cyan arrows). This ghost reflection is related to the subsurface layer located at 4–6 m depth. It shows a generally horizontal layer with constant thickness except at horizontal distances 1560–1660 m, where the retrieved ghost reflection indicates local thinning. Based on known geology, we interpret this change in the thickness of this specific layer as possibly indicating the appearance of the sand layer at this depth. It is, therefore, possible to use such retrieved ghost reflection for imaging and monitoring of the shallow subsurface.

DISCUSSION

Applying SI using surface reflection data results in the appearance of ghost reflections in the retrieved virtual-source or virtual-receiver gathers. The ghost reflections
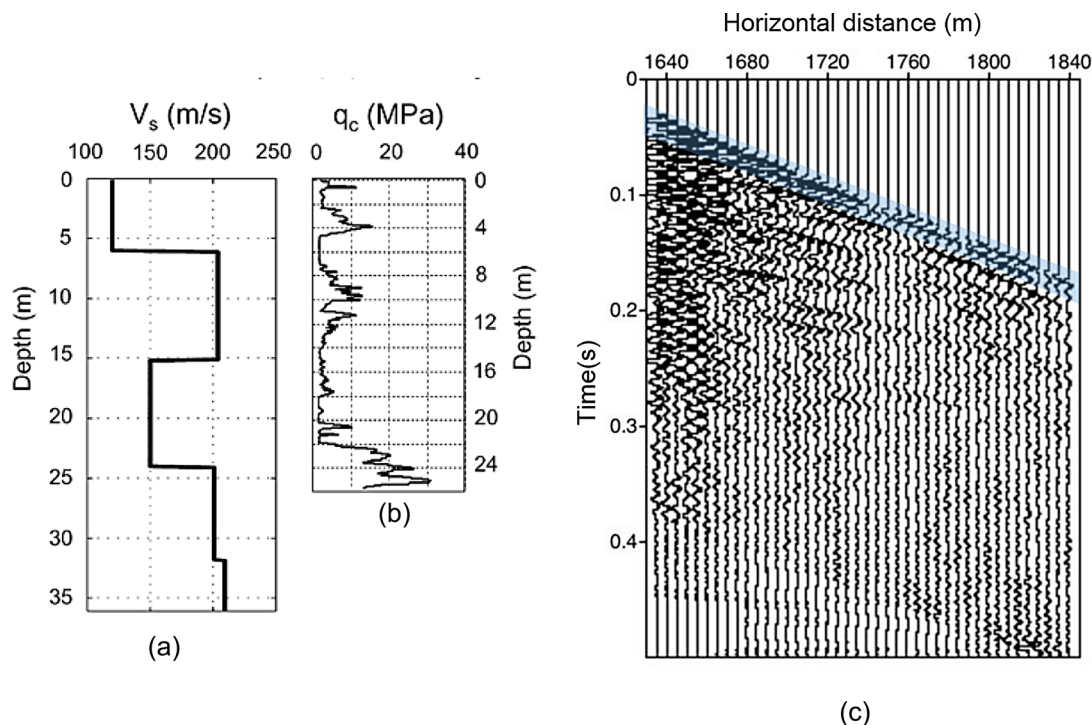
EAGE EUROPEAN ASSOCIATION OF GEOSCIENTISTS & ENGINEERS

FIGURE 5   (a) Interval velocity obtained from the root-mean-square velocity, and (b) the CPT cone-tip resistance at the same site (Ghose and Goudswaard, 2004). (c) Example of an active-source shot gather, where the source is located at 1635 m (the blue highlighted region shows the extracted reflection arrivals used for SI by AC).
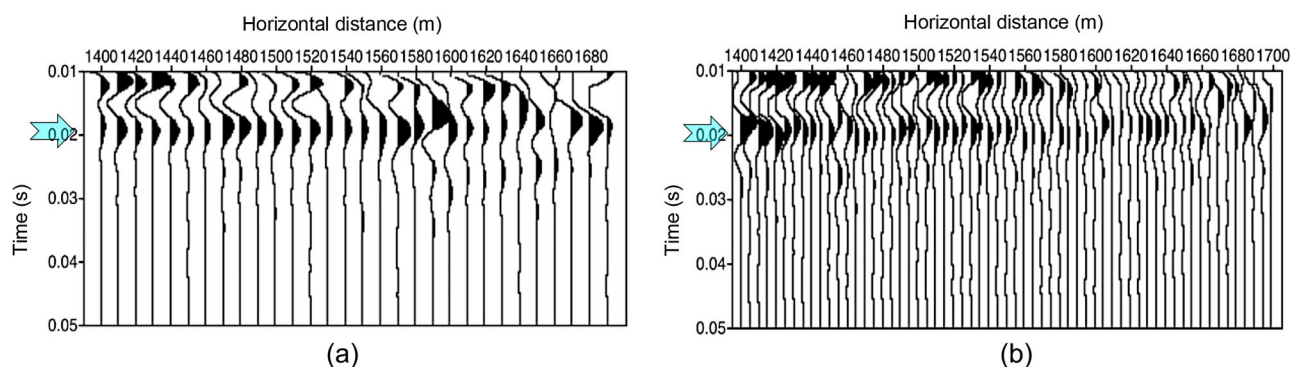

FIGURE 6   Result of seismic interferometry (SI) by auto-correlation (AC) applied to field data: (a) to turn active sources into virtual receivers and (b) to turn the receivers into virtual sources. The cyan arrows indicate the retrieved ghost reflection.

result from the correlation of the primary reflections from different depth levels. These ghost reflections are comparable to the spurious multiples as described by Snieder et al. (2006) for one-sided illumination, to virtual refractions (Nichols et al., 2010) and also to ghost reflections due to intrinsic losses (Draganov et al., 2013).

Our study was designed to determine the application of ghost reflections for monitoring and imaging purposes for shallow subsurface applications. In the previous section, we showed that we could successfully retrieve a ghost reflection from the field dataset. The ghost reflection indicated a horizontal layer with constant thickness except at greater horizontal distances, where it indi-

cated local thinning. Using a ghost zero-offset section directly allows us to make such an interpretation, as the retrieved ghost reflections depend kinematically only on the properties of the layer (or layers) that caused them to be retrieved. Draganov et al. (2013) showed that applying SI for the retrieval of ghost reflections eliminates the kinematic influence of the layers above the target one. This means that any possible kinematic influence of the layers above the target layer in the field data is eliminated.

Ghose and Goudswaard (2004) showed a stacked time section of the subsurface structures for the same field data in Figure 6. They obtained the stacked section

through careful data processing, including surface-related multiple elimination as mentioned above, but also careful velocity analysis for normal-moveout correction and stacking. In Figure 6, one can also observe that the layer between 60 ms and 100 ms exhibits local thinning between common-midpoint numbers 670 and 700. This is also the target layer for which we retrieved the ghost zero-offset section in Figure 6. Our results actually confirm that the local thinning is indeed real and not caused by less accurate velocity picking for layers above the target one. This comparison shows that the stacked time section or depth section can be utilized for interpreting the changes in ghost reflections by observing the specific primary reflections used for retrieving ghost reflections. However, they cannot be directly employed for a straightforward comparison with the retrieved ghost reflections because the ghost reflections can only be observed in the virtual zero-offset section retrieved from SI (by AC). We show the comparison of the zero-offset section obtained directly from full active-source data for the subsurface model shown in Figure 2a, and the virtual zero-offset section retrieved from SI by AC in Appendix A.

We showed the first application of ghost reflections in shallow subsurface studies. We applied SI to turn receivers into virtual sources and to turn shots into virtual receivers. Choosing one and/or the other would depend on the used acquisition geometry of a dataset that is available, for example on shot and receiver spacings and on the number of traces in common-receiver and common-source gathers.

As mentioned earlier, the result of SI by AC is a zero-offset section which is retrieved without any other processing. The results we showed are obtained for a horizontally layered medium. It is also possible to retrieve ghost reflections in complex structures, such as faults, dipping layers and pinch-outs (Shirmohammadi et al., 2022; Draganov et al., 2012). Moreover, the significant advantage of ghost reflections being only sensitive to the changes inside the layer that caused them to appear in the SI results makes the developed methodology for the retrieval of ghost reflections very interesting not only for monitoring shallow subsurface structures, but also for the deep structure such as fluid reservoirs or temporal and cyclic storage of H_2 and CO_2.

We showed that eliminating the surface-related multiples and muting all other events, specifically the primary reflections from the top and bottom of the target layer(s), results in retrieved ghost reflections that are clearer and more robust (see Figure 3e,f in comparison with Figure 3d and b,c). However, extracting reflection signals from both the top and bottom of the target layer from a field dataset requires those events to be clearly interpretable in the field dataset. This might pose a challenge due to interference with surface waves, surface-related multiples, and other undesired events, highlighting a constraint in our suggested approach. Therefore, it is

advisable to implement careful data processing prior to SI, as demonstrated in our field dataset example. Nevertheless, for specific subsurface situations, the retrieved ghost reflections could still be contaminated by artefacts in some receiver locations because of the effect of other undesired reflections in the active-source gathers (Figure 4b,c(ii)). Therefore, it is worth mentioning that for some conditions where retrieving a strong ghost reflection of a specific layer is problematic, it is also possible to look at the ghost reflections which propagate inside more than one layer, such as the one shown in Figure 4a–e(ii).

We also applied SI by CC, which resulted in retrieved multi-offset gathers (see Appendix B). The results of SI by CC are particularly important for further use of ghost reflections in velocity analysis for estimating the velocity inside specific layers. We attempted to apply velocity analysis to the SI results on the field dataset, but the result was not very stable. The reason for this might be the low, and thus insufficient, number of traces in the retrieved common-midpoint gathers. Therefore, using a fixed receiver geometry in field acquisitions for the application of SI for the retrieval of ghost reflections is recommended.

CONCLUSION

We investigated the application of ghost reflections for shallow subsurface imaging and monitoring purposes. We retrieved ghost reflections using SI by AC applied to seismic reflection data recorded with active sources and receivers at the surface.

Using a numerically modelled dataset for a horizontally layered subsurface, we illustrated that the retrieved ghost reflections can be used to monitor changes in a specific layer that causes the ghost reflections to appear in the SI results. Additionally, we proposed to eliminate the surface-related multiples in the active-source gathers and mute undesired events before applying SI to improve the retrieval of the ghost reflections.

We applied the methodology for retrieval of ghost reflections using SI by AC to shallow subsurface SH-wave data acquired at a site located close to Rotterdam, the Netherlands. The retrieved zero-offset section directly showed the geometry of a layer at a depth of 4–6 m. The retrieved virtual zero-offset section allowed the interpreting of the local thinning of this specific layer. Our study can be helpful in other ghost-reflection applications in monitoring and/or imaging shallow or deeper subsurface structures.

DATA AVAILABILITY STATEMENT

The data that support the findings of this study are available on request from the authors.

ORCID

Faezeh Shirmohammadi https://orcid.org/0000-0002-4423-5579

REFERENCES

Boullenger, B. & Draganov, D. (2016) Interferometric identification of surface-related multiples. *Geophysics*, 81(6), Q41–Q52. https://doi.org/10.1190/GEO2015-0450.1

Brouwer, J., Ghose, R., Helbig, K., & Nijhof, V. (1997). The improvement of geotechnical subsurface models through the application of S-wave reflection seismic exploration. 3rd EEGS Meeting. https://doi.org/10.3997/2214-4609.201407288

Curtis, A., & Halliday, D. (2010). Directional balancing for seismic and general wavefield interferometry. *GEOPHYSICS*, 75(1), SA1–SA14. https://doi.org/10.1190/1.3298736

Curtis, A., Nicolson, H., Halliday, D., Trampert, J. & Baptie, B. (2009) Virtual seismometers in the subsurface of the Earth from seismic interferometry. *Nature Geoscience*, 2(10), 700–704. https://doi.org/10.1038/ngeo615

Draganov, D., Heller, K. & Ghose, R. (2012) Monitoring CO_2 storage using ghost reflections retrieved from seismic interferometry. *International Journal of Greenhouse Gas Control*, 11, S35–S46. https://doi.org/10.1016/j.ijggc.2012.07.026

Draganov, D., Ghose, R., Heller, K. & Ruigrok, E. (2013) Monitoring changes in velocity and Q using non-physical arrivals in seismic interferometry. *Geophysical Journal International*, 192(2), 699–709. https://doi.org/10.1093/gji/ggs037

Draganov, D., Ghose, R., Ruigrok, E., Thorbecke, J. & Wapenaar, K. (2010) Seismic interferometry, intrinsic losses and Q-estimation. *Geophysical Prospecting*, 58(3), 361–373. https://doi.org/10.1111/j.1365-2478.2009.00828.x

Ghose, R., Brouwer, J. & Nijhof, V. (1996) A portable S-wave vibrator for high-resolution imaging of the shallow subsurface. In: *58th EAGE Conference and Exhibition, Amsterdam, The Netherlands, June 3–7*, Utrecht: European Association of Geoscientists & Engineers, pp. 1–2.

Ghose, R. & Goudswaard, J. (2004) Integrating S-wave seismic-reflection data and cone penetration-test data using a multiangle multiscale approach. *Geophysics*, 69(2), 440–459. https://doi.org/10.1190/1.1707064

Ghose, R. (2012) A microelectromechanical system digital 3C array seismic cone penetrometer. *Geophysics*, 77, WA99–WA107

Halliday, D.F., Curtis, A., Robertsson, J.O. & Van Manen, D.-J. (2007) Interferometric surface-wave isolation and removal. *Geophysics*, 72(5), A69–A73. https://doi.org/10.1190/1.2761967

Harmankaya, U., Kaslilar, A., Thorbecke, J., Wapenaar, K. & Draganov, D. (2013) Locating near-surface scatterers using non-physical scattered waves resulting from seismic interferometry. *Journal of Applied Geophysics*, 91, 66–81. https://doi.org/10.1016/j.jappgeo.2013.02.004

King, S., & Curtis, A. (2012). Suppressing nonphysical reflections in Green's function estimates using source-receiver interferometry. *GEOPHYSICS*, 77(1), Q15–Q25. https://doi.org/10.1190/geo2011-0300.1

King, S., Curtis, A. & Poole, T.L. (2011) Interferometric velocity analysis using physical and nonphysical energy. *Geophysics*, 76(1), SA35–SA49. https://doi.org/10.1190/1.3521291

Löer, K., Meles, G.A., Curtis, A. & Vasconcelos, I. (2013) Diffracted and pseudo-physical waves from spatially limited arrays using source-receiver interferometry (SRI). *Geophysical Journal International*, 196(2), 1043–1059. https://doi.org/10.1093/gji/ggt435

Ma, Xu, Kirichek, A., Heller, K. & Draganov, D. (2022) Estimating P- and S-wave velocities in fluid mud using seismic interferometry. *Frontiers in Earth Science*, 10, 1–11. https://doi.org/10.3389/feart.2022.806721

Ma, Xu, Kirichek, A., Shakeel, A., Heller, K. & Draganov, D. (2021) Laboratory seismic measurements for layer-specific description of fluid mud and for linking seismic velocities to rheological properties. *The Journal of the Acoustical Society of America*, 149(6), 3862–3877. https://doi.org/10.1121/10.0005039

Nichols, J., Mikesell, D. & Van Wijk, K. (2010) Application of the virtual refraction to near-surface characterization at the Boise Hydrogeophysical *Research Site*. *Geophysical Prospecting*, 58(6), 1011–1021. https://doi.org/10.1111/j.1365-2478.2010.00881.x

Ruigrok, E.N., Wapenaar, K., Van Der Neut, J.R. & Draganov, D.S. (2009) A review of crosscorrelation and multidimensional deconvolution seismic interferometry for passive data. In: Passive Seismic Workshop: Case Studies and Applications for Field Development and Exploration Utrecht: European Association of Geoscientists and Engineers, 1–7.

Ruigrok, E., Campman, X., Draganov, D. & Wapenaar, K. (2010) High-resolution lithospheric imaging with seismic interferometry. *Geophysical Journal International*, 183(1), 339-357. https://doi.org/10.1111/j.1365-246X.2010.04724.x17

Shirmohammadi, F., Draganov, D., Balestrini, F. & Ghose, R. (2022) Application of seismic interferometry with non-physical reflections using near-surface seismic field data. In: NSG2022 28th European Meeting of Environmental and Engineering Geophysics. Utrecht, European Association of Geoscientists and Engineers. pp. 1–5. https://doi.org/10.3997/2214-4609.202220075

Snieder, R., Miyazawa, M., Slob, E., Vasconcelos, I. & Wapenaar, K. (2009) A comparison of strategies for seismic interferometry. *Surveys in Geophysics*, 30(4–5), 503–523. https://doi.org/10.1007/s10712-009-9069-z

Snieder, R., Wapenaar, K. & Larner, K. (2006) Spurious multiples in seismic interferometry of primaries. *Geophysics*, 71(4), SI111–SI124. https://doi.org/10.1190/1.2211507

Thorbecke, J.W. & Draganov, D. (2011) Finite-difference modelling experiments for seismic interferometry. *Geophysics*, 76(6), H1–H18. https://doi.org/10.1190/geo2010-0039.1

van Groenestijn, G.J. & Verschuur, D.J. (2009) Estimating primaries by sparse inversion and application to near-offset data reconstruction. *Geophysics*, 74(3), A23–A28. https://doi.org/10.1190/1.3111115

Verschuur, D.J., (1991) Surface-related multiple elimination: an inversion approach [Ph.D. thesis]. Delft University of Technology. http://resolver.tudelft.nl/uuid:09df29e2-9487-4fe6-87e0-c2a9470933d7

Wapenaar, K. & Fokkema, J. (2006) Green's function representations for seismic interferometry. *Geophysics*, 71(4), SI33–SI46. https://doi.org/10.1190/1.2213955
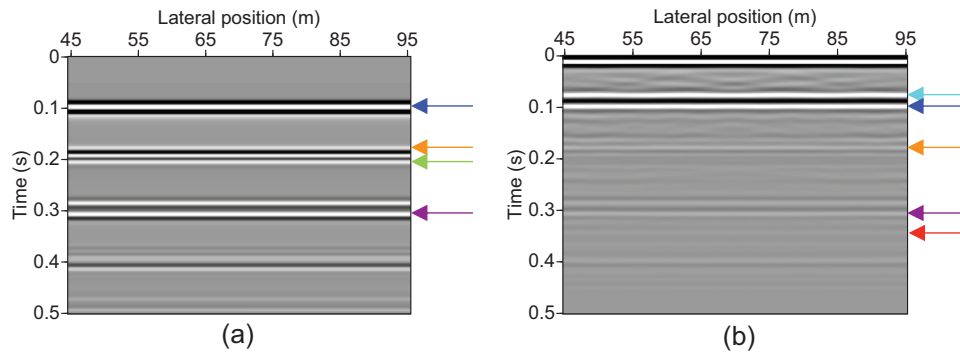
FIGURE A1   (a) The zero-offset section obtained using the full active-source data for the subsurface model shown in Figure 2a, (b) the virtual zero-offset section retrieved from seismic interferometry (SI) by auto-correlation (AC) using the full active-source gathers.

APPENDIX A

The comparison of the virtual zero-offset section retrieved from seismic interferometry by auto-correlation (SI by AC) with the zero-offset section obtained using active-source data

Figure A1a shows the zero-offset gathers obtained directly from full active-source data for the subsurface model shown in Figure 2a without any processing. We can see various primary reflections, such as those from the bottom of the first, second and third layers (marked by the blue, orange and purple arrows, respectively), as well as free-surface multiples (for illustration, one marked by the green arrow). Figure A1a can be directly compared with Figure A1b, which is the virtual zero-offset section obtained from seismic interferometry (SI) by AC using full active-source data. Comparing these two sections, we can see that several horizontal reflections are retrieved in the virtual zero-offset section, both pseudo-physical and ghost reflections. The pseudo-physical reflections exhibit kinematics similar to those of reflection events in the active-source reflection data (marked by the blue, orange and purple arrows). But we can only observe ghost reflections in the virtual zero-offset gathers, such as the ghost reflection from inside the second layer (marked by the cyan arrow in Figure A1b) and the ghost reflection from the combination of the second and third layers (marked by the red arrow in Figure A1b).

APPENDIX B

Ghost reflections retrieved from seismic interferometry by cross-correlation (SI by CC)

Besides SI by auto-correlation (AC), we applied SI by CC. We used the synthetic dataset, like the active-source gather in Figure 2b, to retrieve a virtual-source gather for a virtual source at 70 m. We applied the CC and summation process from relation (2) to all the modelled active-source gathers. Here, we show the summation of the casual and acausal parts of the retrieved responses. We can do that as we expect the causal and

acausal times to be symmetric around $t = 0$ s because there are active sources and receivers on both sides of the virtual source. If, for example, the virtual source is chosen at the position of one of the left-most receivers, most of the useful retrieved arrivals (pseudo-physical and ghost reflections) will be retrieved at acausal times (Ruigrok et al., 2010), and thus, only the acausal part can be used.

Figure B1a shows the retrieved virtual-source gather for a virtual source at 70 m using SI by CC. It shows that we retrieve different arrivals from the subsurface layers, including pseudo-physical and ghost reflections; the yellow arrows at 0.12 and 0.21 s for a horizontal distance of 70 m in Figure B1a indicate interference of such reflections. In general, the pseudo-physical reflections result from the correlation of primaries with their surface-related multiples, whereas the ghost reflections are the result of the correlation of primaries, internal multiple or their combination. For example, the correlation of the primary reflection from the bottom of the first layer (the blue arrow in Figure 2b) with its free-surface multiple (the green arrow in Figure 2b) results in the retrieval of the pseudo-physical reflection from the bottom of the first layer. On the other hand, the correlation of the primary reflection from the bottom of the first layer (the blue arrow in Figure 2b) with the primary reflection from the bottom of the third layer (the purple arrow in Figure 2b) results in the retrieval of a ghost reflection that appears to have propagated only inside the second and third layers. However, identifying the ghost reflections might be challenging when the full recordings are used for SI by CC, as can be seen in Figure B1a, because different retrieved arrivals interfere with each other.

As mentioned in the RESULTS section, one way to make the result of SI clearer for interpretation of the ghost reflections is to mute the arrivals recorded before and after the reflections that contribute to the retrieval of specific target ghost reflections. Figure B1b shows the result retrieved from SI by CC for a virtual source at 70 m when we used reflection panels with muted arrivals
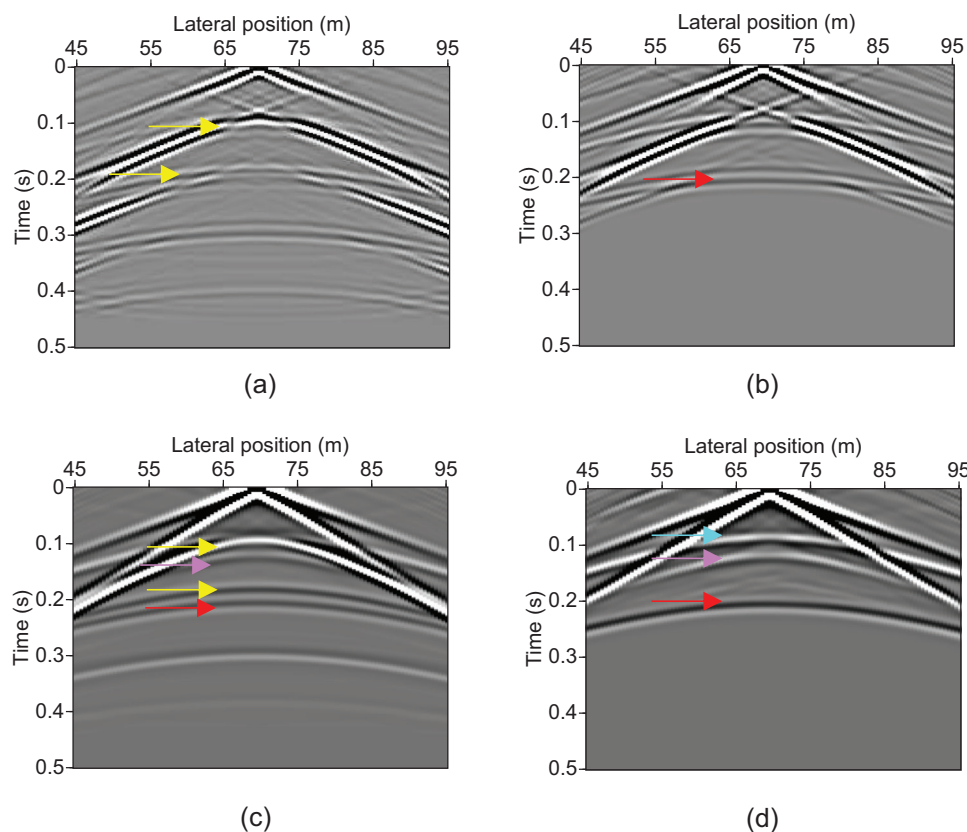
FIGURE B1 (a) Retrieved results of seismic interferometry (SI) by cross-correlation (CC) for a virtual source at (70, 0) m (b) as in (a), but for active-source gathers which are muted before the reflection from the bottom of the first layer and after the reflection from the bottom of the third layer, (c and d) same as (a and b) but when the model has an absorbing boundary condition at the surface. The colour-coded arrows indicate the events described in Table 1.

before the reflection from the bottom of the first layer (the arrival indicated by the blue arrow in Figure 2b) and after reflection from the bottom of the third layer (the arrival indicated by the purple arrow in Figure 2b).

Comparing the result in Figure B1b with the result in Figure B1a, we can see that the retrieved ghost reflection in Figure B1b (the red arrow) is clearer and more robust, which is a result of selecting and correlating specific arrivals in the recorded reflection panels. This ghost reflection results from the correlation of the primary reflections from the bottom of the first and the third layers (the blue and the purple arrows in Figure 2b, respectively).

As in the RESULTS section, we applied SI by CC to the modelled common-source gathers where an absorbing boundary condition is defined at the surface, like the one in the example of active-source gather in Figure 2c. Figure B1c exhibits the resulting virtual common-source gather for a virtual source at 70 m. The observed events are all ghost reflections, but some of them interfere with each other (the yellow arrows). Nevertheless, the ghost reflection from inside the third layer (the pink arrow in Figure B1c) and the ghost reflection from inside the

second and the third layers are retrieved clearer than in Figure B1a (the red arrow in Figure B1c). Thus, to retrieve even clearer ghost reflections that propagate inside specific target layers, it is better to mute the events other than the primary reflections in the active-source gathers, as we did before.

Figure B1d shows the result retrieved from SI by CC for a virtual source at 70 m for muted arrivals before the reflection from the bottom of the first layer (the blue arrow in Figure 2c) and after the reflection from the bottom of the third layer (the purple arrow in Figure 2c). Comparing Figure B1d with Figure B1c, we can see we retrieve clearer, that is better ghost reflections. Such is the ghost reflection from the second layer at 0.09 s for the receiver at 70 m (the cyan arrow in Figure B1d, which is a result of the correlation of the primary reflections from the top and the bottom of the second layer (the blue and the orange arrows in Figure 2c). We can also distinguish the ghost reflection from inside the third layer at 0.12 s for the receiver at 70 m (the pink arrow in Figure B1d) and the ghost reflection from inside the second and the third layers at 0.21 s for the receiver at 70 m (the red arrow in Figure B1d).